

ARTICLE

Received 24 Mar 2016 | Accepted 25 Nov 2016 | Published 13 Jan 2017

DOI: 10.1038/ncomms14062

OPEN

Heterogeneity in mantle carbon content from CO₂-undersaturated basalts

M. Le Voyer^{1,†}, K.A. Kelley², E. Cottrell³ & E.H. Hauri¹

The amount of carbon present in Earth's mantle affects the dynamics of melting, volcanic eruption style and the evolution of Earth's atmosphere via planetary outgassing. Mantle carbon concentrations are difficult to quantify because most magmas are strongly degassed upon eruption. Here we report undegassed carbon concentrations from a new set of olivine-hosted melt inclusions from the Mid-Atlantic Ridge. We use the correlations of CO₂ with trace elements to define an average carbon abundance for the upper mantle. Our results indicate that the upper mantle carbon content is highly heterogeneous, varying by almost two orders of magnitude globally, with the potential to produce large geographic variations in melt fraction below the volatile-free solidus. Such heterogeneity will manifest as variations in the depths at which melt becomes interconnected and detectable, the CO₂ fluxes at mid-ocean ridges, the depth of the lithosphere-asthenosphere boundary, and mantle conductivity.

¹Carnegie Institution of Washington, Department of Terrestrial Magnetism, 5241 Broad Branch Road NW, Washington, District Of Columbia 20015-1304, USA. ²Graduate School of Oceanography, University of Rhode Island, Narragansett Bay Campus, Narragansett Rhode Island 02882, USA. ³Smithsonian Institution, National Museum of Natural History, PO Box 37012, MRC 119, Washington, District Of Columbia 20013-7012, USA. † Present address: Department of Geology, University of Maryland, 8000 Regents Drive, College Park, Maryland 20742, USA. Correspondence and requests for materials should be addressed to M.L.V. (email: mlevoyer@umd.edu).

The carbon content of undegassed mid-oceanic ridge basalts (MORB) and of the upper mantle has been an ongoing debate for several decades^{1–9}. Carbon is a volatile element that plays a key role in major geodynamical processes such as mantle melting and volcanic degassing. The amount of carbon present in the mantle will affect the onset of deep melting, the geophysical properties of the mantle, as well as long-term climate change when CO₂ is released into the atmosphere¹. Because of its very low solubility¹⁰, magmatic degassing depletes carbon in the melt during ascent and eruption, which prevents direct measurements of the original carbon content of most basaltic melts formed in equilibrium with the mantle source. Previous studies have used indirect approaches to correct for degassing, such as isotopic fractionation models, vesicle size distribution or the composition of the gas trapped in vesicles^{2,3,5}. Our knowledge of mantle carbon is best constrained by direct measurements of only two undegassed samples: the popping rock 2πD43 (ref. 2) and the Siqueiros melt inclusions⁴. Together these two samples show correlations between CO₂ content and non-volatile trace elements (such as Nb) that directly constrain the amount of carbon in the upper mantle^{2,4}, and thus both samples have served as references for CO₂ fluxes due to volcanism and its effect on long-term climate changes¹¹. Yet, the two most recent studies of these samples^{2,4} show that their CO₂/Nb ratios differ by more than a factor of two, suggest that the mantle CO₂/Nb ratio is either variable² or constant⁴, and propose upper mantle CO₂ abundances and mid-ocean ridge CO₂ fluxes that vary by a factor of four. Another study reports unusually high CO₂ contents in melt inclusions from the Juan de Fuca ridge¹². However the decoupling between their CO₂ and Nb contents indicates that part of the CO₂ was lost through degassing before entrapment¹². A recent study¹³ compiled most CO₂ measurements from published MORB glasses and melt inclusions, along with new data from 15 ultradepleted MORB glasses that are undersaturated in CO₂ and do not contain any vesicles. Because of this, the authors argue that they are mostly undegassed¹³. These undersaturated MORB glasses have average CO₂/Rb, CO₂/Ba and CO₂/Nb ratios that are close to those of the Siqueiros melt inclusions, also ultradepleted⁴. Studies of additional undegassed samples are critical to understanding whether these differences are due to sampling bias or real geologic variability.

Here we report the CO₂ contents of an independent set of olivine-hosted melt inclusions from the equatorial Mid-Atlantic Ridge (MAR). Using correlations between CO₂ and highly incompatible elements, we show that these melt inclusions represent another rare occurrence of undegassed MORB, and

we discuss the implications of our results with respect to the carbon content of the mantle and the carbon flux from the global ridge system.

Results

Description of the sample. We analysed the major, trace and volatile elements of Fo_{86–90} olivine-hosted melt inclusions from the glassy rim of a pillow basalt from the equatorial MAR. Sample EN061-5D-3A was dredged on-axis by R/V *Endeavor* in 1981 (5.185° S, 11.517° W) (refs 14–16). The host glass is a depleted MORB with La/Sm_N = 0.5, similar to the average depleted MORB composition (D-MORB, La/Sm_N = 0.5 (refs 17,18)). The matrix glasses contain 0.118 ± 0.004 wt% H₂O, 206 ± 14 p.p.m. CO₂, 102 ± 5 p.p.m. F, 1,014 ± 66 p.p.m. S and 17.8 ± 2.0 p.p.m. Cl (uncertainty is 2 s.d. on replicate analyses from 15 glass chips), which is typical for a depleted MORB erupted at ~3,300 m below sea level. The matrix glasses are saturated to slightly oversaturated with respect to a CO₂-rich vapour phase at the pressure of eruption. Their estimated pressure of vapour saturation is P_{sat} = 444 ± 30 bar (ref. 10).

Description of the melt inclusions. From this sample we analysed 23 melt inclusions for major, trace and volatile element content; all of the melt inclusions are free of shrinkage bubbles. They are glassy, tholeiitic basalts with MgO contents slightly higher than their host glasses. All but three of the melt inclusions have undergone <3% post entrapment crystallization (PEC), and so although we refer herein to their PEC-corrected chemistry, the correction is inconsequential to our results (see Methods). Incompatible minor and trace element contents range from highly depleted to compositions identical to those of the matrix glass.

Trace element composition of the melt inclusions. We used the high-resolution trace element data set to assess which process is responsible for the large range and co-variation of the highly incompatible element contents in the equatorial Atlantic melt inclusions^{19–23}. In a plot of C^H/C^M versus C^M, where C^H and C^M are the concentrations of a highly incompatible trace element such as Rb or Th and a moderately incompatible element such as Nd, partial melting is expressed as a straight line with a slope > 1, while fractional crystallization would produce an almost horizontal line, and mixing would produce a curve¹⁹. In Fig. 1a, we see that the equatorial MAR melt inclusions plot on a straight line that is not horizontal, ruling out fractional crystallization as a main relationship explaining the range in

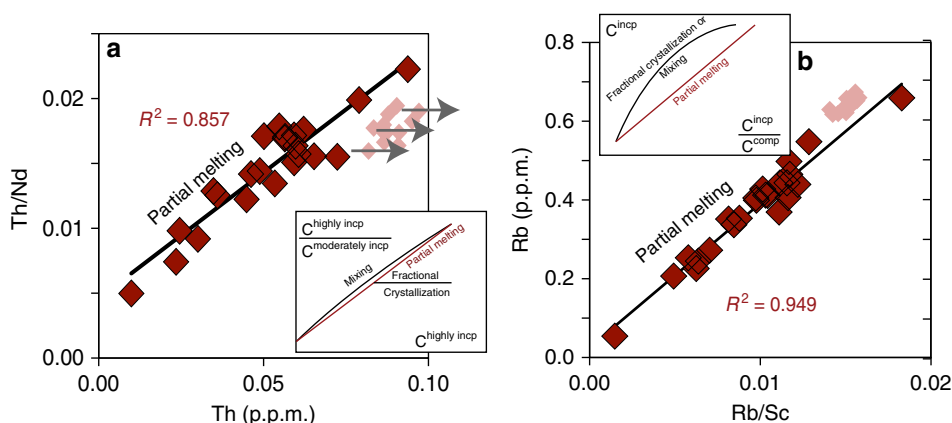


Figure 1 | Variation in trace element composition of the equatorial MAR melt inclusions. (a) Th/Nd ratio as a function of Th content (p.p.m.) for the equatorial melt inclusions (red diamonds) and matrix glasses (pink diamonds). (b) Rb content (p.p.m.) as a function of Rb/Sc ratio for the equatorial MAR melt inclusions and matrix glasses.

composition of these melt inclusions. The small range in the major element contents of the melt inclusions (Supplementary Table 1) support this conclusion as well. Similarly, in a plot of C^H versus C^H/C^C , where C^C is the concentration of a compatible element such as Sc, mixing and crystallization would produce hyperbolic curves, while partial melting would generate a straight line¹⁹. In Fig. 1b, the straight line defined by the equatorial Atlantic melt inclusions confirms that they are related by variable degrees of melting. However we cannot rule out mixing as a possible cause for the large range in trace element compositions. The range in degree of melting calculated from the major element compositions (11–23%, using $Na_{(8)}$ following ref. 24) is too small to account for the range in incompatible elements observed in the equatorial Atlantic melt inclusions (for example, Rb contents vary from 0.05 to 0.66, a 12-fold increase) using a simple batch melting model of a DMM-type mantle source²⁵. The range in incompatible elements can be easily reproduced by modelling compositions of incremental melts produced during fractional melting, using a melt fraction varying from 0.7 to 1.0% (ref. 26). The range in incompatible trace element compositions could also reflect variable amounts of mixing between very low degree incremental melts early in the melting process (highly enriched in incompatible trace elements, such as the carbon-rich melts formed at depth beneath oceanic ridges¹), and aggregated melts produced later in the melting process by $\sim 14\%$ of melting. The incomplete pooling of melts is similar to the process described for the Famous segment²⁷, where some of the melt inclusions trapped in olivines record compositions systematically more depleted than the matrix glasses. Alternatively, the large variation in trace elements could reflect a variable source composition, that is, a heterogeneous source containing a trace-element depleted source and a trace-element enriched source with up to ~ 10 -fold enrichment of the most incompatible trace elements compared to the depleted source. However, the compositions of the matrix glasses do not represent an average of the compositions of the melt inclusions, because the matrix glasses are most likely melt batches that are more enriched than the incremental melts preserved as melt inclusions. The absence of melt inclusions that record compositions more enriched than the matrix glass could reflect the fact that melt inclusions preferentially sample high degree melts²⁷. Another hypothesis is that the matrix glasses are early-formed melts that mixed before cooling and olivine crystallization, while the melt inclusions are late-formed melts that are available in an unmixed form to be trapped in olivine. We favour the scenario of mixing of incremental melt batches produced from a single source at variable depths and variable degree of melting (that is, a deep melting event above the dry carbonated peridotite solidus, that produces very low degree

melts, highly enriched in carbon and other trace elements, and another, more shallower melting event, above the dry peridotite solidus, that produces higher degree melts of the same source previously depleted by the first deep melting event¹).

Volatile element composition of the melt inclusions. The melt inclusions contain 68–719 p.p.m. CO_2 , 52–90 p.p.m. F, 779–1,087 p.p.m. S, 1.6–17.7 p.p.m. Cl and 0.10–0.14 wt% H_2O . Compared to the matrix glasses, which have suffered from strong CO_2 degassing typical of most MORB glasses, the saturation pressures of the melt inclusions reflect minimum entrapment depths down to 4 km below the sea floor ($P_{sat} = 150$ –1,500 bar). Because we do not observe shrinkage bubbles in the melt inclusions, the measured contents for the other volatiles, particularly CO_2 , represent those of the melts at the time they were trapped in olivine. The large range in volatile content is consistent with the range in other incompatible trace elements found in the melt inclusions. In Fig. 2a, we see that the equatorial MAR melt inclusions span a large range of Ce contents, similarly to other incompatible trace elements. However, H_2O , which partitions similarly to Ce (ref. 28) only spans a very limited range of concentration (0.10–0.14 wt%), with an average H_2O content in the melt inclusions identical to that of the matrix glass (0.118 ± 0.004 wt%). At the depth of eruption ($\sim 3,300$ m.b.s.l.), water degassing is only minimal (the equilibrium vapour phase contains < 0.3 mol% of H_2O); thus H_2O/Ce should not be affected by degassing. Because most melt inclusions are depleted in trace elements compared to the matrix glasses, they should record lower H_2O contents as well. The similar H_2O contents recorded in the melt inclusions and the matrix glass illustrates a late-stage H_2O enrichment in these depleted melt inclusions, by diffusive re-equilibration of hydrogen²⁹ between the H_2O -depleted melt inclusions and the H_2O -rich matrix glasses, most likely during storage and differentiation in a shallow magma reservoir before eruption. If we assume that all melt inclusions had a H_2O/Ce ratio similar to those of the matrix glasses (245 ± 12), we can reconstruct the initial H_2O content of the melt inclusions (0.03–0.12 wt% H_2O , average of 0.07 wt% H_2O). The amount of H_2O gain through diffusion varies from none up to 2.8 times compared to the estimated initial H_2O contents. We report in Fig. 2b the Cl content of the melt inclusions and matrix glasses as a function of their Nb content. Unlike most MORB samples, which tend to show variable amounts of seawater-derived Cl contamination, and therefore a variable Cl/Nb, the equatorial Atlantic melt inclusions have a constant Cl/Nb ratio of 14.3 ± 3.8 . A similar value is recorded in the matrix glasses. This indicates that the equatorial melt inclusions as well as matrix glasses did

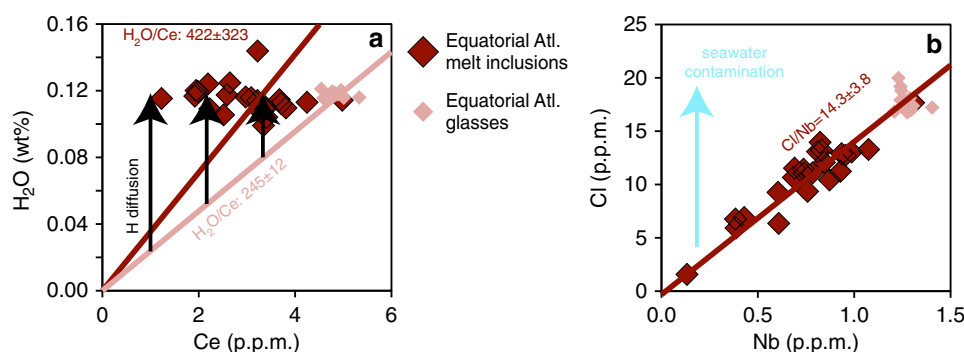


Figure 2 | Behaviour of H_2O and Cl in the equatorial MAR melt inclusions. (a) Variation in H_2O content (wt%) as a function of Ce content (p.p.m.) for the equatorial MAR melt inclusions and matrix glasses. (b) Variation in Cl content (p.p.m.) as a function of Nb content (p.p.m.) for the equatorial melt inclusions and matrix glasses.

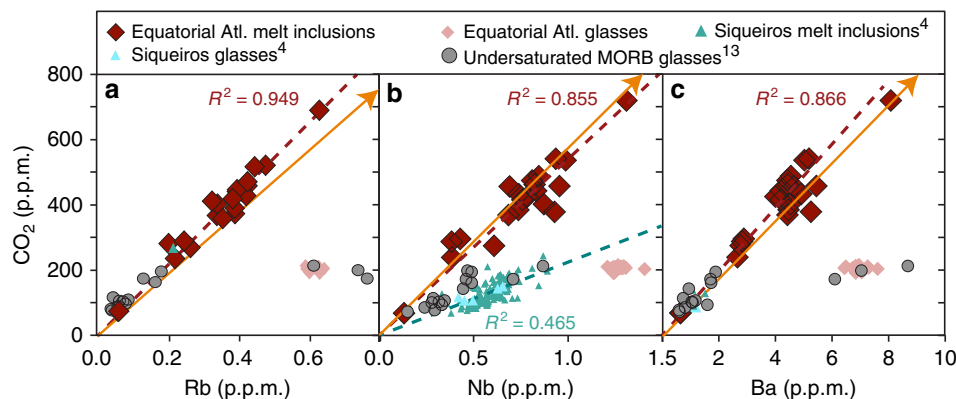


Figure 3 | Variations in CO₂ content as a function of highly incompatible trace elements. The CO₂ content of the equatorial MAR melt inclusions and matrix glasses is represented as a function of Rb (a), Nb (b) and Ba (c), for, and compared to the Siqueiros melt inclusions and matrix glasses⁴, the popping rock (outside of the scale, represented by the arrow, CO₂ and Nb (ref. 2); Rb and Ba (ref. 31)), and the undersaturated ultradepleted MORB glasses¹³. The single Siqueiros Rb point represents an average calculated using the Rb and Ba correlation found in Siqueiros melt inclusions⁴⁸, applied to the maximum Ba measured in Siqueiros melt inclusions⁴. R^2 values refer to the linear regressions (dashed lines) through each set of samples.

Table 1 | Average values for the CO₂/Rb, CO₂/Ba and CO₂/Nb ratios.

	CO ₂ /Rb	CO ₂ /Ba	CO ₂ /Nb
Equatorial MIs	1105 ± 104	97 ± 10	557 ± 79
Equatorial glasses	320 ± 14	30 ± 2	162 ± 8
Siqueiros MIs (ref. 4)	1219 ± NA	100 ± 22	239 ± 46
Siqueiros glasses ⁴	NA	68 ± NA	224 ± 45
Popping Rock ²	899 ± 91	76 ± 8	556 ± 56
undersaturated ultradepleted MORB glasses ¹³	1207 ± 633	89 ± 39	249 ± 48
global average for MORB glasses ¹³	NA	105 ± 9	607 ± 327

For the equatorial melt inclusions/glasses, the Siqueiros melt inclusions/glasses and the undersaturated ultradepleted MORB glasses, the 1 s.d. uncertainty is the standard deviation over the entire population of melt inclusions. For the popping rock, the uncertainty is calculated using the standard deviation over three measurements of CO₂ content² and a conservative error of 10% relative for trace elements.

not suffer from significant alteration or assimilation of hydrothermal material³⁰.

Correlation between CO₂ and other trace elements. The CO₂ content of the melt inclusions strongly correlates with other highly incompatible elements such as Ba, Rb and Nb, which indicates that these melt inclusions did not lose their initial carbon through degassing (Fig. 3). Note that the CO₂ content of the equatorial melt inclusions also strongly correlates with their Cl content (CO₂/Cl = 39 ± 4, 2 s.d., linear regression of $R^2 = 0.912$). For comparison, the CO₂/Cl ratio of Siqueiros melt inclusions is 77 ± 26 (ref. 4), and the CO₂/Cl ratio of popping rock is 46 (ref. 2). However the CO₂/Cl ratio was not used below because, although the equatorial melt inclusions do not show any signs of seawater contamination, most MORB samples do. Therefore the use of the CO₂/Cl ratio as a source proxy cannot be generalized to the global scale, as most MORB samples are strongly contaminated with seawater-derived Cl (ref. 30). The average CO₂/Rb and CO₂/Ba ratios of the equatorial Atlantic melt inclusions (1,105 ± 104 and 97 ± 10, Table 1) are only slightly higher than those for the popping rock 2πD43, and very similar to those for Siqueiros melt inclusions (Table 1, Fig. 3). The average CO₂/Nb ratio of the equatorial MAR melt inclusions (557 ± 79) is identical to the popping rock 2πD43, but approximately two times higher than the Siqueiros melt inclusions (Table 1; Figs 3 and 4). The equatorial MAR melt inclusions have a CO₂/Rb and CO₂/Ba ratios that are indistinguishable from those of the undersaturated MORB glasses¹³, and a CO₂/Nb ratio that is 50% higher. The similarity between the undersaturated MORB

glasses¹³ and our undegassed melt inclusions reinforces the conclusion that these undersaturated MORB glasses are mostly undegassed as well, although three out of their 15 glasses have lower CO₂ content for a given Rb, Ba or Nb and might be degassed (Fig. 3).

Discussion

Carbon is present as carbonate in the uppermost mantle under the oxidizing conditions relevant for the formation of MORB (refs 4,31). Because very small extents of melting will efficiently remove carbonate minerals from the source, further melting will only dilute carbon in the pooled magma. The CO₂-Nb correlation found in the Siqueiros melt inclusions indicates that C partitions similarly to Nb during melting and crystallization⁴. However, a recent experimental study found C to be slightly more incompatible than Nb, closer to Ba and Rb, and thus CO₂/Nb is not a perfect canonical ratio at low degrees of melting⁶. Observations from a global compilation on MORB glasses also suggest that Ba is the best proxy for C to model the CO₂ content of MORB and of the suboceanic mantle¹³. Nonetheless, at the degrees of melting typical of MORB generation, nearly all of the CO₂, Rb, Ba and Nb from the mantle source are contained in the MORB melt, and thus CO₂/Ba, CO₂/Rb and CO₂/Nb are all indicative of MORB source composition⁶. The correlations found between CO₂ contents and highly incompatible trace element contents in the equatorial MAR melt inclusions (Fig. 3) confirm this observation. In the following, we use all three ratios in combination in order to assess the mantle CO₂ content at the global scale.

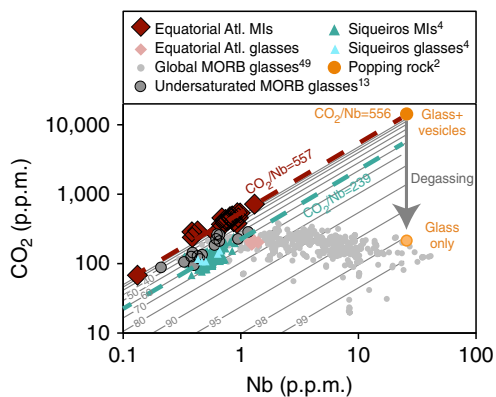


Figure 4 | Variation in CO₂ content as a function of Nb content. Red dashed line: average CO₂/Nb in the equatorial MAR melt inclusions. The Siqueiros melt inclusions⁴ (green dashed line: average CO₂/Nb) and matrix glasses⁴, the popping rock² and the undersaturated ultradepleted MORB glasses¹³ are also plotted for comparison. The matrix glasses from both Siqueiros and equatorial MAR samples plot consistently with the global MORB glass database⁴⁹, affected by variable amounts of carbon degassing (thin grey lines, graduated in % of CO₂ loss, assuming an initial undegassed CO₂/Nb of 557).

Although it is unlikely that carbon is homogeneously distributed in the upper mantle⁷, an average CO₂ content is useful for many planet-scale geochemical and geophysical models. The average trace element composition of the equatorial MAR melt inclusions from this study is representative of the uppermost oceanic mantle away from any hotspot influence¹⁷. Similarly, the radiogenic isotope composition of the host glass¹⁴ is representative of average depleted MORB mantle (DMM). Thus, the values for CO₂/Rb, CO₂/Ba and CO₂/Nb ratios measured in the equatorial MAR melt inclusions should be representative of the DMM as well, as opposed to Siqueiros melt inclusions⁴ and the ultradepleted MORB glasses¹³, which are highly depleted, and to the Popping Rock², which is highly enriched. We used a compilation of Rb, Ba and Nb contents for global mantle averages from the literature (DMM values^{25,32} and DMM calculated from global MORB averages^{17,18,33–35}, assuming that Rb, Ba and Nb are completely incompatible, and using an average melting degree of 10%) together with the CO₂/Rb, CO₂/Ba and CO₂/Nb ratios from the equatorial MAR melt inclusions (Table 1). We obtain a global average CO₂ in the mantle source of 137 ± 54 p.p.m. CO₂ (1 s.d. over the range in Rb, Ba and Nb from the literature estimates), equivalent to 37.4 ± 14.7 p.p.m. C. The result is identical within error regardless of which ratio is used (CO₂/Ba, CO₂/Rb, or CO₂/Nb). This CO₂ abundance is within the range of previously determined abundances for the DMM from MORB of the Northern Atlantic province (~ 175 p.p.m. (ref. 2), using an average CO₂/Nb of 530, a MORB Nb content of 3.31 p.p.m., and assuming an average degree of melting of 10%), that determined from global MORB compilations (60–183 p.p.m. (ref. 13)), and lies between the estimates from the Siqueiros melt inclusions (72 ± 19 p.p.m. (ref. 4), or 36 p.p.m. (ref. 32)) and the popping rock 2πD43 (~ 300 p.p.m. (ref. 5)). Our value is twice as high as the average CO₂ content of the mantle estimated from vesicle size distribution (66–78 p.p.m. (ref. 3)). The discrepancies between models show that these values are highly sensitive to which value of Rb, Ba or Nb, and which melting model is used¹³.

Assuming that our estimate of 137 ± 54 p.p.m. CO₂ is representative of the average DMM CO₂ content, we calculate an average CO₂ flux from ridges of $1.8 \pm 0.7 \times 10^{12}$ mol yr⁻¹, using a MORB flux of $21 \text{ km}^3 \text{ yr}^{-1}$ (ref. 36), and an average

degree of melting of 10%. The uncertainty on this estimate is conservative, as it takes into account the range in estimates of the Ba, Rb and Nb concentrations in DMM. This CO₂ flux corresponds to an average ³He flux released from ridges of 802 ± 316 mol yr⁻¹, using a constant CO₂/³He ratio for MORB of $2.2 \pm 0.7 \times 10^9$ (refs 8,9). The calculated CO₂ flux is in very good agreement with previous estimates based on popping rock 2πD43 (2.3×10^{12} mol yr⁻¹ (ref. 2)), and is twice as high as estimated from Siqueiros melt inclusions ($9.3 \pm 2.8 \times 10^{11}$ mol yr⁻¹ (ref. 4)). Our CO₂ flux is higher than the global estimates from vesicularity (6.5 ± 1.8 to $8.7 \pm 2.8 \times 10^{11}$ mol yr⁻¹ (ref. 3)), and is slightly lower than those from a global MORB glass compilation ($2.8 \pm 0.4 \times 10^{12}$ mol yr⁻¹ (ref. 13)). Normalized by the total length of the ridge system (60,864 km (ref. 17)), this corresponds to an average CO₂ flux of $2.9 \pm 1.1 \times 10^7$ mol yr⁻¹ km⁻¹. However, the CO₂ flux from each segment of the global mid-ocean ridge system may vary as a function of magma flux and mantle source CO₂ content. In the case of the ridge segment where sample EN061-5D-3 A was dredged, the local spreading rate of 3.26 mm yr^{-1} (ref. 17) and crustal thickness of 5 km (ref. 14) translate to a local magma flux of $0.0168 \text{ km}^3 \text{ yr}^{-1}$, a local CO₂ flux of $1.4 \pm 0.6 \times 10^9$ mol yr⁻¹, and a local ³He flux of 0.64 ± 0.25 mol yr⁻¹. Normalized by the length of the ridge segment (segment MAR179, 103 km long¹⁷), the local CO₂ flux corresponds to an average flux of $1.4 \pm 0.5 \times 10^7$ mol yr⁻¹ km⁻¹, which is half the average global flux. Thus, the differences observed between local and global CO₂ fluxes illustrate geographical variations of at least a factor of two in the CO₂ flux from ridges, controlled by variations in mantle carbon concentration and magma flux. This observation agrees with independent estimates based on MORB vesicularity³.

The equatorial MAR melt inclusions, an example of depleted MORB, have ratios of CO₂/Ba, CO₂/Rb and CO₂/Nb very similar to the popping rock 2πD43, which is a highly enriched MORB (Fig. 3, Table 1). This observation demonstrates that these ratios are not simple functions of the amount of trace element enrichment or depletion in MORB; however, the limited range in these ratios, even taking Siqueiros into account, shows that absolute mantle CO₂ abundances will scale with mantle Ba, Rb and Nb abundances. In order to successfully capture the global range of the upper mantle CO₂ content, we use the global Rb, Ba and Nb variations from the literature, together with the CO₂/Rb, CO₂/Ba and CO₂/Nb ratios from the equatorial MAR melt inclusions (Table 1). We selected estimates of Rb, Ba and Nb contents in both depleted MORB sources (D-DMM) and enriched MORB sources (E-DMM) (refs 17,32), and obtain a range in DMM CO₂ content of 20–1,200 p.p.m., equivalent to 5.5–327 p.p.m. C. This range, reflecting the full spectrum of depleted-to-enriched MORB sources, is wider than previously reported and covers almost two orders of magnitude, including the low^{4,13,25} and the high² mantle CO₂ estimates. This range is in good agreement with the global range estimated independently from vesicle size distribution (27–999 p.p.m. CO₂ (ref. 3)). Our high CO₂ end-member is higher than anything previously reported, and indicates that enriched mantle sources could contain much more carbon than previously suggested. This wide range in CO₂ content shows the extent of carbon heterogeneity that is present in the mantle, and demonstrates that mantle source composition is an important contributor to the geographical variations in ocean ridge CO₂ fluxes discussed above.

In a procedure similar to that for CO₂, we provide estimates for the H₂O, Cl and F content of the DMM. We do not apply this approach to S because the EN061-5D-3Ag are sulfide-saturated³⁷; therefore, their S content is a direct function of the FeO content of the melt and cannot be linked to the S content of the mantle

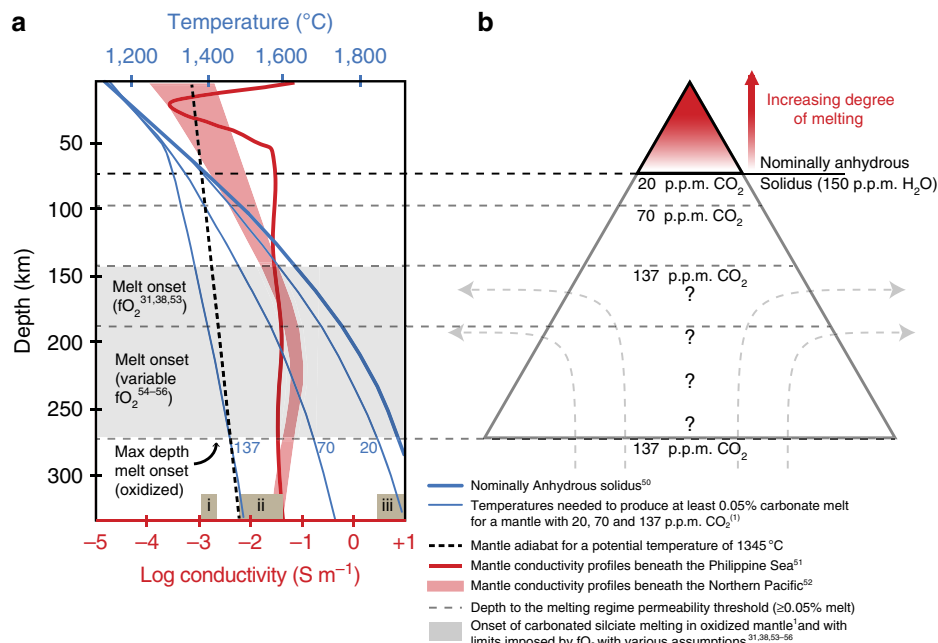


Figure 5 | Simplified model of mantle melting. (a) Variation of melting temperatures with depth as a function of mantle CO₂ content (blue curves)^{2,50}, and electrical conductivity versus depth (red curves) for the upper mantle beneath the Philippine Sea⁵¹ (thin red curve) and north Pacific⁵² (broad red curve). Shaded boxes at the base of the plot represent the range of laboratory electrical conductivity measurements for dry olivine (i), olivine containing 150 p.p.m. H₂O (ii) and melt (iii) (refs 30,50). (b) Schematic cross-section of the permeable melting regime beneath a mid-ocean ridge based on a, using the same vertical scale, a mantle potential temperature of 1,345°C and a permeability threshold of 0.05%. At depths below the nominally anhydrous solidus, melting is dominated by small fractions of carbonate and carbonated silicate melt. Shaded grey zones indicate possible, depths for carbonated silicate melt initiation depending on the oxygen fugacity (f_{O_2}) of the mantle^{53–56}. Onset at the carbonated silicate solidus¹ assumes that mantle f_{O_2} is high enough to stabilize carbonate over diamond at 275 km. If the mantle is more reducing, melting will instead initiate at the f_{O_2} -dependent diamond to carbonate transition. Melt initiation between 140 and 180 km encompasses whole rock $Fe^{3+}/\Sigma Fe$ ratios from 0.035 to 0.05 based on the continental xenolith record³⁸—depths that are also consistent with a range of MORB $Fe^{3+}/\Sigma Fe$ ratio, Fe^{3+} bulk partition coefficients, and primitive mantle Fe_2O_3 contents¹⁹ and the assumption that 37 p.p.m. C has the power to reduce $Fe^{3+}/\Sigma Fe$ by >1% as it oxidizes to carbonate. Because the subsolidus $Fe^{3+}/\Sigma Fe$ ratio of the mantle and the depth of metal saturation are uncertain, the depth of melt initiation is also uncertain.

source. Water from the equatorial melt inclusions suffered from diffusive re-equilibration with the host glass, through H diffusion. Therefore we used the H₂O content of the matrix glasses instead. We used a compilation of global averages for the mantle Ce, Nb and Zr contents from the literature (DMM values^{25,32} and DMM calculated from global MORB averages^{17,18,33–35}), together with the H₂O/Ce ratio from the equatorial matrix glasses (244 ± 12 , 1 s.d.), and the Cl/Nb and F/Zr ratios from the equatorial melt inclusions (Table 1). We obtained a global average of H₂O, Cl and F contents in the mantle source of 238 ± 68 p.p.m., 4.1 ± 1.2 p.p.m. and 22 ± 5 p.p.m., respectively. These values are higher than the DMM values of 142 ± 85 p.p.m. H₂O, 1.0 ± 0.5 p.p.m. Cl and 16 ± 3 p.p.m. F estimated from the Siqueiros melt inclusions⁴ as well as the DMM values of 0.5 p.p.m. Cl and 11 p.p.m. F (ref. 25).

Our results on the CO₂ content of the DMM have important implications for the geophysical detection of melt in the upper mantle and the origin of the asthenosphere. Provided that oxygen fugacity is high enough to stabilize carbonate³⁸, carbonate melting will begin wherever the mantle temperature exceeds the carbonated mantle solidus, producing a melt fraction that is a function of the amount of CO₂ in the mantle¹. At the MORB mantle CO₂ contents that we have constrained, this melt fraction will be vanishingly small. However, carbonate melts can become interconnected at very low melt fractions, as small as 0.05% (ref. 39), and thus there exists a melt fraction threshold below which carbonate melts cannot be extracted from the mantle and would not be detectable by geophysical methods. This threshold melt fraction can be used to define the effective base of the

melting regime beneath ridges as well as the effective depth of melting. The seismic low-velocity zone beneath oceanic plates⁴⁰ and the electrical conductivity structure of the upper mantle⁴¹ are both thought to be due to the presence of melt beneath the lithosphere. In particular, carbonate melts are highly conductive, much more so than hydrated mantle or silicate melts⁴². Using petrologic estimates for the reduction in melting temperature as a function of CO₂ content¹, a mantle potential temperature of 1,345°C and an interconnection threshold of 0.05% in melt fraction³⁹, we show that the regional variations in upper mantle CO₂ that we have documented here predict large variations in the depth to the effective base of the melting regime beneath ridges, which should correlate with geochemical trace element signatures of depletion and enrichment in MORB (Fig. 5). An upper mantle source with a CO₂ abundance of 20 p.p.m. would produce 0.005% melt, which is an order of magnitude below the threshold for interconnection³⁹ and would, in areas of trace element depletion, predict an absence of melt and low electrical conductivity at depths deeper than the nominally anhydrous mantle solidus (85 km (ref. 1)). A less depleted MORB source with 70 p.p.m. CO₂, such as the source for Siqueiros MORB, would produce enough carbonated silicate melt to establish an interconnected (and thus conductive) network of melt at depths of ~95 km and above. An average MORB source with 137 p.p.m. CO₂ would produce an interconnected network of carbonated silicate melt throughout the entire upper mantle, limited at its base only by redox freezing where carbonate is converted to diamond^{1,38} (Fig. 5). Given sufficient depth resolution of electrical conductivity measurements, it may be possible to use

geophysical measurements to determine the depth to the effective base of the carbonated melting regime in areas of trace element depletion, and the depth to the carbonate-diamond transition in areas of trace element enrichment. Given that the carbonate-diamond transition is dependent on oxygen fugacity^{1,38}, variations in the depth of this redox boundary—if resolved—could be indicative of lateral variations in the oxygen fugacity of the mantle.

Methods

Sample preparation. We selected olivine grains that contained fully entrapped melt inclusions, with no cracks or links to the outside glass. We mounted the olivine grains in epoxy and polished them using SiC papers in order to expose the melt inclusions. After polishing, we removed the grains from epoxy using a soldering iron, pressed them into an indium mount, and polished the indium mounts using first diamond paste, then 1/3 μm alumina paste. We washed the mounts using alcohol and water, then stored them for >48 h in a vacuum oven at 70 °C, before applying a gold coat.

Volatile elements. We first analysed the volatile element compositions (H_2O , CO_2 , F, Cl and S) of the matrix glass and the melt inclusions using the NanoSIMS Cameca 50L at the Department of Terrestrial Magnetism, Carnegie Institution, following the procedure described in ref. 43. We used a 12–13 nA, Cs⁺ primary beam to presputter the sample using a $30 \times 30 \mu\text{m}^2$ raster, then performed the analysis using a $10 \times 10 \mu\text{m}^2$ raster, and collected data on the central $3.8 \times 3.8 \mu\text{m}^2$ of the crater, measuring 5 blocks of 10 analyses each. We assessed blank under these conditions by replicate measurements on Suprasil 3,002 glass and synthetic forsterite, which yield values of 0.2 p.p.m. CO_2 , 2 p.p.m. H_2O and <0.05 p.p.m. F, Cl and S. Typical analytical error (2 s.d. over n analytical cycles) are <3% rel. for all volatiles. We assessed uncertainties by measuring basaltic glass ALV519-4-1 every 10 analyses, which yield uncertainties of 7% rel. for CO_2 and <5% rel. for all other volatiles (2 s.d. over 50 analyses during a 4-day long analytical session). Supplementary Table 1 shows the long-term uncertainties as 2 s.d. external reproducibility of repeated measurements in four basaltic standards.

Major elements. After measuring volatile elements, we slightly polished the samples using 1/3 μm alumina powder in order to remove the gold coat, then we applied a carbon coat. We measured the major element compositions of the host olivines, the matrix glasses and the melt inclusions using a JEOL electron microprobe at the Geophysical Laboratory, Carnegie Institution, using the following conditions: 15 kV accelerating voltage, 30 nA beam, spot mode (for the olivine) or beam defocused to 10 μm diameter (for the glasses). We processed the olivine analyses for matrix correction using the set of absorption coefficients from ref. 44. Supplementary Table 2 shows replicate measurements in basaltic glass standard VE-32. Supplementary Table 3 shows the major element compositions of the olivines.

Trace elements. Finally, we analysed the concentrations of 40 trace elements in the melt inclusions and the matrix glasses by Laser-Ablation Inductively Coupled Mass Spectrometry at the Department of Terrestrial Magnetism, Carnegie institution, following methods adapted from refs 45,46. We used a Photon Machines UV laser coupled with a Thermo iCapQ quadrupole ICP-MS. We ran the analyses using 100% energy output, 20 Hz repeat rate and 50 μm spot size. We normalized the data to ²⁹Si as the internal standard. We used a set of 11 mafic glass standards (BIR-1g, BCR-2g, BHVO-2g, GSC-1g, GSD-1g, GSA-1g, BM90-21g, GOR132-g, GOR128-g, KL2-g and ML3B-g) to perform the calibration (linear regressions with $r^2 > 0.995$). We assessed uncertainties and analytical drift using repeated measurement of basaltic glass standard VE-32, measured every 10 analyses of unknowns (Supplementary Table 4). We measured each sample three times, and combined accuracy and reproducibility on sample analyses is <10% (2 RSD) on average for all elements, except for Cs and U, whose low contents were close to or below detection levels.

Post-entrapment olivine crystallization. We assessed the major, volatiles and trace element compositions of the melt inclusions for post-entrapment olivine crystallization (PEC). We used a Fe^{3+}/Fe , of 0.16 (average value measured in local MORB glasses³⁷ identical to the global average MORB value³¹), together with the Fe-Mg partition coefficient between olivine and silicate melt⁴⁷. We corrected the melts by adding olivine back to the melt using increments of 0.1%. All melt inclusions indicated an amount of PEC of $\leq 3\%$ of olivine, with the exception of three melt inclusions that indicated PEC of 5, 7 and 9% of olivine. Supplementary Table 5 shows the PEC-corrected compositions of the melt inclusions and matrix glasses. Supplementary Table 6 shows the raw compositions of the melt inclusions and matrix glasses before PEC correction. Note that the main results of this study do not depend on the PEC correction, as both the use of the PEC-corrected compositions and the uncorrected compositions would yield similar conclusions.

Data availability. The authors declare that all data generated during this study are included in this published article (and its Supplementary Information files).

References

- Dasgupta, R. *et al.* Carbon-dioxide-rich silicate melt in the Earth's upper mantle. *Nature* **493**, 211–215 (2013).
- Cartigny, P., Pineau, F., Aubaud, C. & Javoy, M. Towards a consistent mantle carbon flux estimate: insights from volatile systematics ($\text{H}_2\text{O}/\text{Ce}$, δD , CO_2/Nb) in the North Atlantic mantle (14° N and 34° N). *Earth Planet. Sci. Lett.* **265**, 672–685 (2008).
- Chavrit, D., Humler, E. & Grasset, D. Mapping modern CO_2 fluxes and mantle carbon content all along the mid-ocean ridge system. *Earth Planet. Sci. Lett.* **387**, 229–239 (2014).
- Saal, A. E., Hauri, E. H., Langmuir, C. H. & Perfit, M. R. Vapor undersaturation in primitive mid-ocean-ridge basalts and the volatile content of Earth's upper mantle. *Nature* **419**, 451–455 (2002).
- Javoy, M. & Pineau, F. The volatiles record of a 'popping' rock from the Mid-Atlantic Ridge at 14° N: chemical and isotopic composition of gas trapped in the vesicles. *Earth Planet. Sci. Lett.* **107**, 598–611 (1991).
- Rosenthal, A., Hauri, E. H. & Hirschmann, M. Experimental determination of C, F, and H partitioning between mantle minerals and carbonated basalt, CO_2/Ba and CO_2/Nb systematics of partial melting, and the CO_2 contents of basaltic source regions. *Earth Planet. Sci. Lett.* **425**, 77–87 (2015).
- Burnard, P., Reisberg, L. & Colin, A. An observed link between lithophile compositions and degassing of volatiles (He, Ar, CO_2) in MORBs with implications for Re volatility and the mantle C/Nb ratio. *Earth Planet. Sci. Lett.* **395**, 159–167 (2014).
- Marty, B. & Jambon, A. C^3/He in volatile fluxes from the solid Earth: implications for carbon geodynamics. *Earth Planet. Sci. Lett.* **83**, 16–26 (1987).
- Marty, B. & Tolstikhin, I. CO_2 fluxes from mid-ocean ridges, arc and plumes. *Chem. Geol.* **145**, 233–248 (1998).
- Dixon, J. E. & Stolper, E. M. An experimental study of water and carbon dioxide solubilities in mid-oceanic ridge basaltic liquids. Part II: applications to degassing. *J. Petrol.* **36**, 1633–1646 (1995).
- Self, S., Widdowson, M., Thordarson, T. & Jay, A. E. Volatile fluxes during flood basalt eruptions and potential effects on the global environment: a Deccan perspective. *Earth Planet. Sci. Lett.* **248**, 518–532 (2006).
- Hélo, C., Longpré, M.-A., Shimizu, N., Clague, D. A. & Stix, J. Explosive eruptions at mid-ocean ridges driven by CO_2 -rich magmas. *Nat. Geosci.* **4**, 260–263 (2011).
- Michael, P. J. & Graham, P. J. The behavior and concentration of CO_2 in the suboceanic mantle: inferences from undegassed ocean ridge and ocean island basalts. *Lithos* **236–237**, 338–351 (2015).
- Schilling, J.-G., Hanan, J. B., McCully, B., Kingsley, R. H. & Fontignie, D. Influence of the Sierra Leone mantle plume on the equatorial Mid-Atlantic Ridge: A Nd-Sr-Pb isotopic study. *J. Geophys. Res.* **99**, 12005–12028 (1994).
- Graham, D. W. *et al.* Helium isotope geochemistry of mid-ocean ridge basalts from the South Atlantic. *Earth Planet. Sci. Lett.* **110**, 133–147 (1992).
- Kelley, K. A., Kingsley, R. H. & Schilling, J.-G. Composition of plume-influenced mid-ocean ridge lavas and glasses from the Mid-Atlantic Ridge, East Pacific Rise, Galápagos Spreading Center, and Gulf of Aden. *Geochem. Geophys. Geosys.* **14**, 223–242 (2013).
- Gale, C. A., Dalton, C. H., Langmuir, Su, Y. & Schilling, J.-G. The mean composition of ocean ridge basalts. *Geochem. Geophys. Geosyst.* **14**, 489–518 (2013).
- Su, Y. J. Mid-Ocean Ridge Basalt Trace Element Systematics: Constraints from Database Management, ICP-MS Analyses, Global Data Compilation, and Petrologic Modeling. PhD thesis, Columbia Univ. (2002).
- Schiano, P., Monzier, M., Eissen, J.-P., Martin, H. & Koga, K. T. Simple mixing as the major control of the evolution of volcanic suites in the Ecuadorian Andes. *Contrib. Mineral. Petrol.* **160**, 297–312 (2010).
- Treuil, M. & Joron, J.-L. Utilisation des éléments hygromagmatophiles pour la simplification de la modélisation quantitative des processus magmatiques: exemples de l'Afar et de la dorsale médio-atlantique. *Soc. Ital. Miner. Petrol.* **31**, 125–174 (1975).
- Allègre, C. J. & Minster, J. F. Quantitative models of trace element behavior in magmatic processes. *Earth Planet. Sci. Lett.* **38**, 1–25 (1978).
- Langmuir, C. H., Vocke, Jr R. D., Hanson, G. N. & Hart, S. R. A general mixing equation with applications to Icelandic basalts. *Earth Planet. Sci. Lett.* **37**, 380–392 (1978).
- Hofmann, A. W. & Feigenson, M. D. Case studies on the origin of Grenada basalts I: theory and reassessment of Grenada basalts. *Contrib. Mineral. Petrol.* **84**, 382–389 (1983).
- Klein, E. M. & Langmuir, C. H. Global correlations of ocean ridge basalt chemistry with axial depth and crustal thickness. *J. Geophys. Res.* **92**, 8089–8115 (1987).
- Salters, V. J. M. & Stracke, A. Composition of the depleted mantle. *Geochem. Geophys. Geosyst.* **5**, Q05B07 (2004).
- Shaw, D. Trace element fractionation during anatexis. *Geochim. Cosmochim. Acta* **34**, 237–243 (1970).

27. Laubier, M., Gale, A. & Langmuir, C. H. Melting and crustal processes at the FAMOUS segment (mid-Atlantic Ridge): new insights from olivine-hosted melt inclusions from multiple samples. *J. Petrol.* **53**, 665–698 (2012).
28. Plank, T., Kelley, K. A., Zimmer, M., Hauri, E. H. & Wallace, P. J. Why do mafic arc magmas contain ~4 wt% water on average? *Earth Planet. Sci. Lett.* **364**, 168–179 (2013).
29. Bucholz, C. E., Gaetani, G. A., Behn, M. D. & Shimizu, N. Post-entrapment modification of volatiles and oxygen fugacity in olivine-hosted melt inclusions. *Earth Planet. Sci. Lett.* **374**, 145–155 (2013).
30. Michael, P. J. & Cornell, W. C. Influence of spreading rate and magma supply on crystallization and assimilation beneath mid-ocean ridges: evidence from chlorine and major element chemistry of mid-ocean ridge basalts. *J. Geophys. Res.* **103**, 18325–18356 (1998).
31. Cottrell, E. & Kelley, K. A. The oxidation state of Fe in MORB glasses and the oxygen fugacity of the upper mantle. *Earth Planet. Sci. Lett.* **305**, 270–282 (2011).
32. Workman, R. K. & Hart, S. R. Major and trace element composition of the depleted MORB mantle (DMM). *Earth Planet. Sci. Lett.* **231**, 53–72 (2005).
33. Hofmann, A. W. Chemical differentiation of the Earth: the relationship between mantle, continental crust, and oceanic crust. *Earth Planet. Sci. Lett.* **90**, 297–314 (1988).
34. Sun, S. S. & McDonough, W. F. Chemical and isotopic systematics of oceanic basalts: implications for mantle composition and processes. *Geol. Soc., Spec. Publ.* **42**, 313–345 (1989).
35. Arevalo, Jr R. & McDonough, W. F. Chemical variations and regional diversity observed in MORB. *Chem. Geol.* **271**, 70–85 (2010).
36. Crisp, J. A. Rates of magma emplacement and volcanic output. *J. Volcanol. Geotherm. Res.* **20**, 177–211 (1984).
37. Le Voyer, M., Cottrell, E., Kelley, K. A., Brounce, M. & Hauri, E. H. The effect of primary versus secondary processes on the volatile content of MORB glasses: An example from the equatorial Mid-Atlantic Ridge (5° N–3° S). *J. Geophys. Res. Solid Earth* **120**, 125–144 (2015).
38. Stagno, V., Ojwang, D. O., McCammon, C. A. & Frost, D. J. The oxidation state of the mantle and the extraction of carbon from Earth's interior. *Nature* **493**, 84–88 (2013).
39. Minarik, W. G. & Watson, E. B. Interconnectivity of carbonate melt at low melt fraction. *Earth Planet. Sci. Lett.* **133**, 423–437 (1995).
40. Kawakatsu, H. *et al.* Seismic evidence for sharp lithosphere-asthenosphere boundaries of oceanic plates. *Science* **324**, 499–502 (2009).
41. Eaton, D. W. *et al.* The elusive lithosphere-asthenosphere boundary (LAB) beneath cratons. *Lithos* **109**, 1–22 (2009).
42. Gaillard, F., Malki, M., Iacono-Marziano, G., Pichavant, M. & Scaillet, B. Carbonatite melts and electrical conductivity in the asthenosphere. *Science* **322**, 1363–1365 (2008).
43. Hauri, E. H. *et al.* SIMS analysis of volatiles in silicate glasses 1. Calibration, matrix effects and comparisons with FTIR. *Chem. Geol.* **18**, 99–114 (2002).
44. Pouchon, J.-L. & Pichoir, F. in *Electron Probe Quantification* (eds Heinrich, K. F. and Newbury, D. E.), 31–75 (Plenum Press, 1991).
45. Kelley, K. A., Plank, T., Ludden, J. & Staudigel, H. Composition of altered oceanic crust at ODP Sites 801 and 1149. *Geochem. Geophys. Geosyst.* **4** (2003).
46. Lytle, M. L. *et al.* Tracing mantle sources and Samoan influence in the northwestern Lau back-arc basin. *Geochem. Geophys. Geosyst.* **13** (2012).
47. Ford, C. E., Russell, D. G., Craven, J. A. & Fisk, M. R. Olivine-liquid equilibria: temperature, pressure and composition dependence of the crystal/liquid cation partition coefficients for Mg, Fe²⁺, Ca and Mn. *J. Petrol.* **24**, 256–265 (1983).
48. Danyushevsky, L. V., Perfit, M. R., Eggins, S. M. & Falloon, T. J. Crustal origin for coupled 'ultra-depleted' and 'plagioclase' signatures in MORB olivine-hosted melt inclusions: evidence from the Siqueiros Transform Fault, East Pacific Rise. *Contrib. Mineral. Petrol.* **144**, 619–637 (2003).
49. Le Voyer, M., Kelley, K. A., Cottrell, E. & Hauri, E. H. Variable carbon degassing from MORB assessed using CO₂/Nb, paper presented at the Goldschmidt Conference, Sacramento, CA, 8–12 June (2014).
50. Hirschmann, M. M. Mantle solidus: experimental constraints and the effects of peridotite composition. *Geochem. Geophys. Geosyst.* **1** (2000).
51. Baba, K. *et al.* Electrical conductivity imaging of the Philippine Sea upper mantle using seafloor magnetotelluric data. *Phys. Earth Planet. Int.* **183**, 44–62 (2010).
52. Lizarralde, D., Chave, A., Hirth, G. & Schultz, A. Northeastern Pacific mantle conductivity profile from long-period magnetotelluric sounding using Hawaii-California submarine cable data. *J. Geophys. Res.* **100**, 17–837 (1995).
53. Bézous, A. & Humler, E. The Fe³⁺/ΣFe ratios of MORB glasses and their implications for mantle melting. *Geochim. Cosmochim. Acta* **69**, 711–725 (2005).
54. Ballhaus, C. Is the upper mantle metal-saturated? *Earth Planet. Sci. Lett.* **132**, 75–86 (1995).
55. O'Neill, H. *et al.* in *Evolution of the Earth and Planets* (eds Takahashi, E., Jeanloz, R. & Rubie, D. C.), 74–88 (Geophys. Monogr. 74, American Geophysical Union, 1993).
56. Rohrbach, A. *et al.* Metal saturation in the upper mantle. *Nature* **449**, 456–458 (2007).

Acknowledgements

The authors acknowledge the support of the Deep Carbon Observatory, Carnegie Institution of Washington and the Smithsonian Institution. We thank Jianhua Wang for the help with the NanoSIMS measurements, Tim Gooding for assistance with sample preparation and John Armstrong for the assistance with EMP measurements. NSF award OCE# 1258771 provides curatorial support for marine geological samples at the Graduate School of Oceanography, University of Rhode Island.

Author contributions

All authors contributed to the design of the study and the writing of the manuscript. K.A.K. obtained the sample from the URI sample collection. M.L.V. prepared the melt inclusions, performed the analyses and processed the data. E.H.H. and E.C. designed Fig. 5.

Additional information

Supplementary Information accompanies this paper at <http://www.nature.com/naturecommunications>

Competing financial interests: The authors declare no competing financial interests.

Reprints and permission information is available online at <http://npg.nature.com/reprintsandpermissions/>

How to cite this article: Le Voyer, M. *et al.* Heterogeneity in mantle carbon content from CO₂-undersaturated basalts. *Nat. Commun.* **8**, 14062 doi: 10.1038/ncomms14062 (2017).

Publisher's note: Springer Nature remains neutral with regard to jurisdictional claims in published maps and institutional affiliations.



This work is licensed under a Creative Commons Attribution 4.0 International License. The images or other third party material in this article are included in the article's Creative Commons license, unless indicated otherwise in the credit line; if the material is not included under the Creative Commons license, users will need to obtain permission from the license holder to reproduce the material. To view a copy of this license, visit <http://creativecommons.org/licenses/by/4.0/>

© The Author(s) 2017